Check for updates

ADVANCED MATERIALS
www.advmat.de

Two-Dimensional $Cs_2AgIn_xBi_{1-x}Cl_6$ Alloyed Double Perovskite Nanoplatelets for Solution-Processed Light-Emitting Diodes

Zhenyang Liu, Yingying Sun, Tong Cai, Hanjun Yang, JinXing Zhao, Tao Yin, Chaoqi Hao, Mingjun Chen, Wenwu Shi, Xiaoxiao Li, Li Guan, Xu Li, Xinzhong Wang, Aiwei Tang, and Ou Chen**

Lead-free double perovskites have emerged as a promising class of materials with potential to be integrated into a wide range of optical and optoelectronic applications. Herein, the first synthesis of 2D $Cs_2AgIn_xBi_{1-x}Cl_6$ ($0 \le x \le 1$) alloyed double perovskite nanoplatelets (NPLs) with well controlled morphology and composition is demonstrated. The obtained NPLs show unique optical properties with the highest photoluminescence quantum yield of 40.1%. Both temperature dependent spectroscopic studies and density functional theory calculation results reveal that the morphological dimension reduction and In–Bi alloying effect together boost the radiative pathway of the self-trapped excitons of the alloyed double perovskite NPLs. Moreover, the NPLs exhibit good stability under ambient conditions and against polar solvents, which is ideal for all solution-processing of the materials in low-cost device manufacturing. The first solution-processed light-emitting diodes is demonstrated using the $Cs_2AgIn_{0.9}Bi_{0.1}Cl_6$ alloyed double perovskite NPLs as the sole emitting component, showing luminance maximum of 58 cd m^{-2} and peak current efficiency of 0.013 cd A^{-1}. This study sheds light on morphological control and composition-property relationships of double perovskite nanocrystals, paving the way toward ultimate utilizations of lead-free perovskite materials in diverse sets of real-life applications.

1. Introduction

Over the past decade, lead halide perovskites (LHPs) with a chemical formula of $APbX_3$ (A: Cs, methylammonium, formamidinium, etc., X: Cl, Br, I) have attracted significant amount of attention in both fundamental research and technological applications owing to their exceptional optical and optoelectronic properties.[1–6] In particular, LHP nanocrystals (NCs) have shown great potential in the field of displays due to a series of merits including tunable bandgap, large exciton binding energy, high emission color purity, facile solution-processability, etc.[7–11] However, two main impediments, that is, toxicity and instability, have significantly hindered further advancements of this class of fascinating materials in a wide spectrum of practical applications.[12,13] Therefore, exploring stable, lead-free perovskite NCs with superior optical performances that are suitable for optical and optoelectronic applications become an emerging research topic in recent years.[14,15] With this intention, double perovskite, a general formula of $A_2M(I)M(III)X_6$, with every two Pb^{2+} cations replaced by a pair of M(I) and M(III) cations has been considered as one of the most promising candidates due to the high electronic dimensionality.[16–24] However, so far, the optical properties of double perovskites are subpar compared to LHPs, mainly due to their large, indirect band gap. Therefore, a rationally designed methodology to tune the electronic structure of double perovskite nanomaterials is a crucial prerequisite for their application in optoelectronic devices.

Composition engineering and morphology control are the two effective means to tune and optimize nanomaterials' properties.[19,25–33] For instance, by partially replacing bismuth with indium for the $Cs_2AgBiCl_6$ double perovskite nanocubes, the initial indirect bandgap can be transited into a direct bandgap, leading to an enhanced absorption cross section, and dramatically increased photoluminescence (PL) quantum yields (QYs).[26,28] In addition, we recently reported a novel synthesis of Cs_2AgBiX_6 (X = Cl, Br, I) double perovskite NCs with a 2D morphology.[34] The resulting $Cs_2AgBiBr_6$ nanoplatelets (NPLs) exhibited significantly improved performance in CO_2 photoreduction reactions comparing to their 0D counterpart,

Z. Liu, Y. Sun, T. Yin, C. Hao, M. Chen, X. Li, L. Guan, X. Li
Hebei Key Laboratory of Optic-Electronic Information and Materials
College of Physics Science and Technology
Hebei University
Baoding 071002, China
Z. Liu, T. Cai, H. Yang, W. Shi, O. Chen
Department of Chemistry
Brown University
Providence, RI 02912, USA
E-mail: ouchen@brown.edu
J. Zhao, A. Tang
Key Laboratory of Luminescence and Optical Information
Ministry of Education
School of Physical Science and Engineering
Beijing JiaoTong University
Beijing 100044, China
E-mail: awtang@bjtu.edu.cn
W. Shi, X. Wang
Institute of Information Technology
Shenzhen Institute of Information Technology
Shenzhen 518172, China

The ORCID identification number(s) for the author(s) of this article can be found under https://doi.org/10.1002/adma.202211235.

DOI: 10.1002/adma.202211235

 © 2023 Wiley-VCH GmbH

$Cs_2AgBiBr_6$ nanocubes.[34] However, dimensional control for multi-component nanocrystals has been quite challenging since it is difficult to balance all the precursors' activities, especially for low temperature nucleation reactions. Up to now, multi-component alloyed double perovskite NPLs have not yet been demonstrated.

Herein, we report the first synthesis of $Cs_2AgIn_xBi_{1-x}Cl_6$ ($0 \le x \le 1$) alloyed double perovskite NPLs. Both experimental results and theoretical calculations confirm that the 2D morphology and In-Bi alloying effect co-facilitate the radiative recombination through self-trapped exciton (STE) states of the $Cs_2AgIn_xBi_{1-x}Cl_6$ double perovskites. A champion PL QY of ≈40% has been reached for $Cs_2AgIn_{0.9}Bi_{0.1}Cl_6$ NPLs. Moreover, we carried out temperature-dependent PL spectroscopic studies and first principles density functional theory (DFT) calculations to unveil the underlying electronic transition mechanism of the 2D alloyed double perovskite NPLs. Furthermore, we show that the obtained NPLs possess excellent stability against moisture and polar solvents, enabling their solution-processing towards device applications. To demonstrate, we solution-processed an NPL-based LED device with a turn-on voltage of 5.5 V and a peak luminance of 58 cd m^{-2}, comparable to the best performances of the state-of-the-art double perovskite-based LEDs produced by conventional thermal vacuum evaporation method.[19,29] Our study provides new and important insights to promote double perovskites and other lead-free perovskite-based materials toward real-world applications.

2. Result and Discussion

The synthetic method of 2D $Cs_2AgIn_xBi_{1-x}Cl_6$ alloyed double perovskite NPLs is derived from our previous work with modifications (see synthetic details in Figure S1, Supporting Information).[34] **Figure 1**A–F shows the transmission electron microscopy (TEM) images of 2D $Cs_2AgIn_xBi_{1-x}Cl_6$ (x = 0.0, 0.3, 0.5 0.7, 0.9, and 1.0) double perovskite NPLs with different compositions. The average lateral sizes of the obtained NPLs with different compositions are in the range of 150–250 nm (Figure S2, Supporting Information). TEM and atomic force microscopy (AFM) measurements revealed that the NPLs possessed an inorganic thickness of ≈3.6 nm with a total thickness of ≈5.1 nm including the surface organic ligand layer (Figure S3, Supporting Information), consistent with our previous study of pure $Cs_2AgBiCl_6$ NPLs.[34] High-angle annular dark-filed (HAADF) scanning TEM (STEM) measurements showed nearly identical image contrast across entire individual NPLs (Figure S4, Supporting Information), further proving the

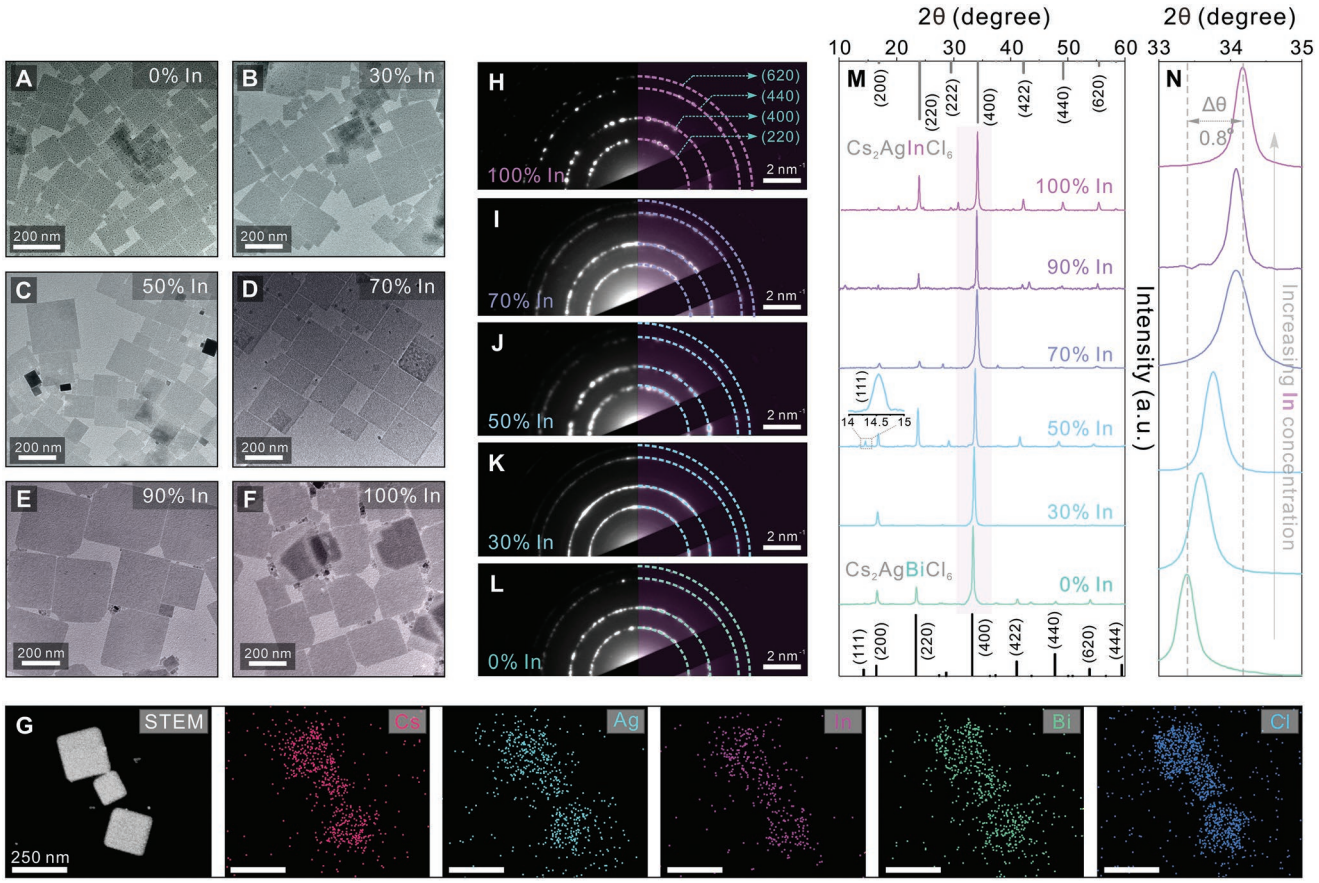

Figure 1. Morphology, composition, and structural characterizations of the $Cs_2AgIn_xBi_{1-x}Cl_6$ double perovskite NPLs. A–F) TEM images of $Cs_2AgIn_xBi_{1-x}Cl_6$ (x = 0, 0.3, 0.5, 0.7, 0.9, and 1) double perovskite NPLs; G) HAADF-STEM image of $Cs_2AgIn_{0.3}Bi_{0.7}Cl_6$ NPLs (left) and the corresponding elemental mapping images for Cs, Ag, In, Bi, and Cl; H–L) SAED patterns for the $Cs_2AgIn_xBi_{1-x}Cl_6$ (x = 0, 0.3, 0.5, 0.7, and 1) NPLs, respectively; M) XRD patterns of the $Cs_2AgIn_xBi_{1-x}Cl_6$ NPLs, and N) the zoomed-in XRD patterns for (400) diffraction peak region (2θ from 33° to 35°) of the double perovskite NPLs.

© 2023 Wiley-VCH GmbH

15214095, 2023, 19, Downloaded from https://onlinelibrary.wiley.com/doi/10.1002/adma.202211235 by Brown University Library, Wiley Online Library on [12/05/2023]. See the Terms and Conditions (https://onlinelibrary.wiley.com/terms-and-conditions) on Wiley Online Library for rules of use; OA articles are governed by the applicable Creative Commons License

15214095, 2023, 19, Downloaded from https://onlinelibrary.wiley.com/doi/10.1002/adma.202211235 by Brown University Library, Wiley Online Library on [12/05/2023]. See the Terms and Conditions (https://onlinelibrary.wiley.com/terms-and-conditions) on Wiley Online Library for rules of use; OA articles are governed by the applicable Creative Commons License

thickness uniformity of the synthesized alloyed double perovskite NPLs. X-ray photoelectron spectroscopy (XPS) spectra of the $Cs_2AgIn_{0.7}Bi_{0.3}Cl_6$ double perovskite NPLs confirmed the existence of all the involved elements, that is, Cs, Ag, In, Bi, and Cl (Figure S5, Supporting Information) with an atomic ratio of Cs:Ag:In:Bi:Cl = 2.0:1.2:0.3:0.6:5.2 (determined by the energy dispersive X-ray spectroscopy), matching well with the precursor feeding ratio (2.0:1.0:0.3:0.7:6.0) as well as the stoichiometry of the double perovskite crystal structure.[26] Elemental mapping analysis showed uniformly distributed In and Bi compositions throughout each individual NPLs (Figure 1G), unambiguously proving an In-Bi alloyed nature of the obtained double perovskite NPLs.

The double perovskite crystal phase of the resulting NPLs was confirmed by high-resolution TEM (HR-TEM), selected area electron diffraction (SAED) and powder X-ray diffraction (XRD) characterizations. A representative HR-TEM image of the $Cs_2AgIn_{0.3}Bi_{0.7}Cl_6$ NPLs showed lattice fringes across the entire NPL, revealing its high crystallinity (Figure S6). The measured *d*-spacing of 2.70 Å can be assigned to that of the (400) crystal plane of double perovskite structure (space group: $Fm\bar{3}m$). The corresponding SAED pattern matched well to the computer simulated pattern (Figure S7, Supporting Information). The SAED for large areas of the $Cs_2AgIn_xBi_{1-x}Cl_6$ (x = 0.0, 0.3, 0.5 0.7, and 1.0) NPLs all showed a good consistency to the double perovskite structure (Figure 1H–L). By gradually substituting Bi component with In, the *d*-spacing of (440) facets were determined by the SAED continuous decreased from 2.69 to 2.61 Å caused by the smaller ionic radii of In^{3+} cation (80 pm) than that of Bi^{3+} cation (103 pm) (Figure S8, Supporting Information).[28] All the XRD patterns of $Cs_2AgIn_xBi_{1-x}Cl_6$ NPLs are shown in Figure 1M. Although the relative Bragg diffraction peak intensity of each NPL sample may differ due to different levels of NPL orientation alignment on the substrate,[34,35] all the XRD patterns can be unambiguously assigned to the elpasolite phase of double perovskite. In addition, with the increase in components, all the XRD peaks shifted to higher diffraction angles (Figure 1N), revealing a shrinkage of the lattice parameter from 10.7 to 10.5 Å, in good accordance with the SAED measurement results (Figure S8, Supporting Information). Interestingly, the XRD pattern of $Cs_2AgIn_{0.5}Bi_{0.5}Cl_6$ NPLs showed a clear (111) Bragg diffraction peak at 14.5°, indicative of a high degree ordering among the M(I) (i.e., Ag^+) and M(III) (i.e., Bi^{3+}, In^{3+}) cationic lattice sites (Figure 1M).[19,28] Altogether, our results manifest the successful synthesis of high-quality 2D $Cs_2AgIn_xBi_{1-x}Cl_6$ alloyed double perovskite NPLs with well controlled and tunable In–Bi compositions.

We next studied the composition effect on the bandgap nature and emission property of the 2D $Cs_2AgIn_xBi_{1-x}Cl_6$ alloyed double perovskite NPLs. The absorption spectrum of $Cs_2AgBiCl_6$ NPLs showed a broad absorption peak around 385 nm (**Figure 2**A), with an indirect bandgap of 2.66 eV determined by Tauc plot analysis on the diffuse reflectance spectrum (Figure S9, Supporting Information).[34] Upon increasing In concentration, the absorption peak at ≈385 nm became narrower and blue-shifted to 368 nm when 90% of Bi^{3+} was replaced by In^{3+} (Figure 2A). Both the gradual disappearance of the long absorption tail and the emergence of a sharp peak at ≈290 nm indicated an indirect-to-direct bandgap transition for the $Cs_2AgIn_xBi_{1-x}Cl_6$ NPLs (Figure 2A).[26] When reaching pure $Cs_2AgInCl_6$ NPLs, only a weak absorption feature at 363 nm can be observed, which was ascribed to the parity-forbidden

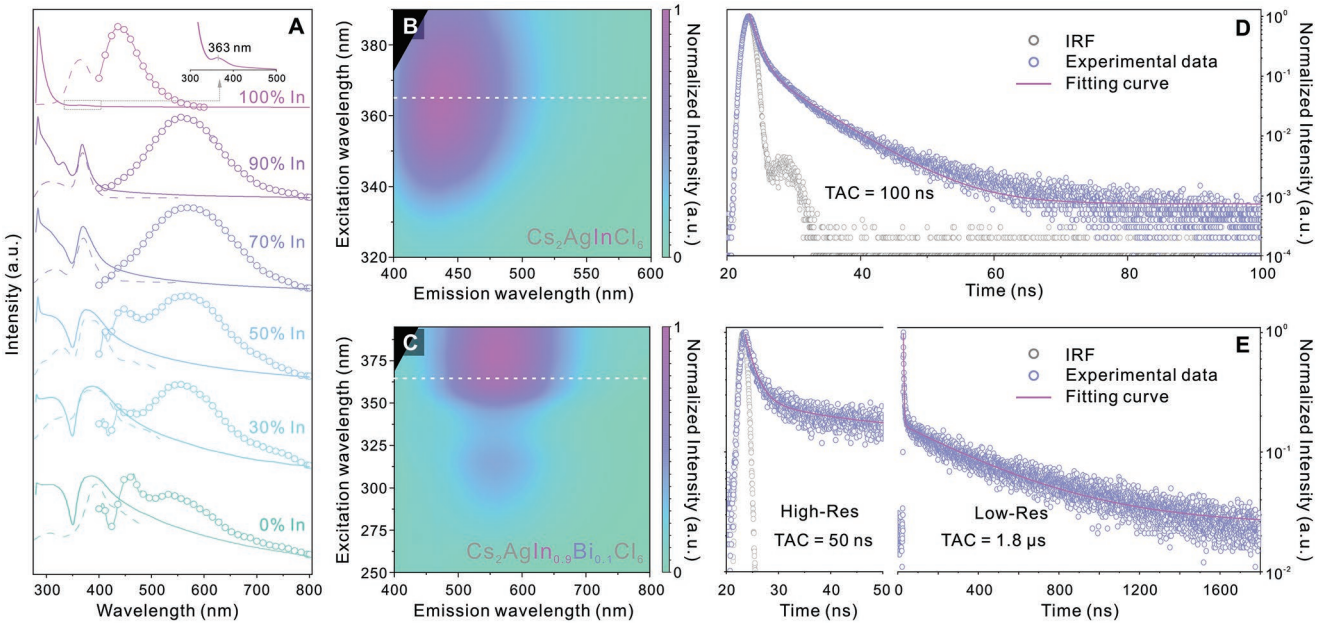

Figure 2. Optical property characterizations of the $Cs_2AgIn_xBi_{1-x}Cl_6$ double perovskite NPLs. A) Absorption (solid line), PL (open circles), and PLE (dash line) spectra of the $Cs_2AgIn_xBi_{1-x}Cl_6$ (x = 0, 0.3, 0.5, 0.7, 0.9, 1) NPLs, the PL spectra were collected under excitation of 365 nm light; 2D pseudo-color contour map of the PL intensity as a function of emission and excitation wavelengths of B) $Cs_2AgInCl_6$ and C) $Cs_2AgIn_{0.9}Bi_{0.1}Cl_6$ NPLs; time-resolved PL decay curves of D) $Cs_2AgInCl_6$ and E) $Cs_2AgIn_{0.9}Bi_{0.1}Cl_6$ NPLs. Instrument response functions (IRF) are plotted in grey circles. Time-to-amplitude converters (TAC) for high and low resolution (High-Res. and Low-Res.) measurements are provided.

 © 2023 Wiley-VCH GmbH

15214095, 2023, 19, Downloaded from https://onlinelibrary.wiley.com/doi/10.1002/adma.202211235 by Brown University Library, Wiley Online Library on [12/05/2023]. See the Terms and Conditions (https://onlinelibrary.wiley.com/terms-and-conditions) on Wiley Online Library for rules of use; OA articles are governed by the applicable Creative Commons License

transition at the band edge of $Cs_2AgInCl_6$ double perovskite (Figure 2A and Figure S10, Supporting Information).[15,36,37] A direct bandgap value of 3.19 eV was determined by Tauc plot analysis of the pure $Cs_2AgInCl_6$ NPLs (Figure S9, Supporting Information), in line with the previous reported studies.[36,37]

Regarding the emission behaviors, all the $Cs_2AgIn_xBi_{1-x}Cl_6$ NPLs with $x \leq 0.50$ showed a weak and broad PL with a low PL QY of <1% (Figure 2A and Figure S11, Supporting Information). The weak PL can be assigned to the self-trapped exciton (STE) emission as previously reported for the double perovskite materials with similar compositions.[19,26,28] However, when the In concentration increased to above 50% (i.e., $x > 0.5$), a drastic increase in the PL intensity and thus PL QY was observed (Figure 2A and Figure S11, Supporting Information). When 90% In was reached, the $Cs_2AgIn_{0.9}Bi_{0.1}Cl_6$ NPLs exhibited a symmetric PL peak centered at 555 nm with a maximal PL QY of 40.1% (Figure 2A and Figure S11, Supporting Information), representing the highest reported value for $Cs_2AgIn_xBi_{1-x}Cl_6$ double perovskite NCs.[21,26,28] The symmetric PL feature with such a high PL QY can be explained by the parity-allowed direct bandgap transition caused by the Bi-inclusion induced crystal-lattice symmetry breaking of the $Cs_2AgIn_{0.9}Bi_{0.1}Cl_6$ alloyed double perovskite.[19,28,29] In addition, the broad emission profile that is similar to other $Cs_2AgIn_xBi_{1-x}Cl_6$ ($x < 0.9$) NPL samples and the linear dependence between the emission intensity and excitation light power suggested the same STE origin for the PL of 2D $Cs_2AgIn_{0.9}Bi_{0.1}Cl_6$ double perovskite NPLs (Figure S12, Supporting Information).[19,27,38] When the Bi component was completely replaced by In (i.e., pure $Cs_2AgInCl_6$ NPLs), the sample exhibited a much bluer PL peak at 436 nm with a dramatically decreased PL QY of ≈2%, which can be explained by reinstalling the lattice symmetry, thus parity-forbiddance of the direct bandgap transition.[27] PL excitation (PLE) spectra of all the NPL samples matched well to the corresponding absorption profiles (Figure 2A), manifesting the band edge electronic transition of double perovskites served as the emission energy origin.[39] The radiative energy relaxation pathways were further proved by 2D pseudo-color contour maps of the PL intensity as a function of excitation and emission wavelength for the $Cs_2AgInCl_6$ and $Cs_2AgIn_{0.9}Bi_{0.1}Cl_6$ NPLs (Figure 2B,C). The maps showed an excitation-independent behavior for both samples, indicating a consistent energy relaxation pathway through the bandgap (STE) for the $Cs_2AgInCl_6$ ($Cs_2AgIn_{0.9}Bi_{0.1}Cl_6$) NPLs under different excitations.[40] Time-resolved PL decay lifetime measurements unveiled an average lifetime of ≈3.7 ns for the $Cs_2AgInCl_6$ NPLs, in line with its direct bandgap electronic transition (Figure 2D and Table S1, Supporting Information).[41] In contrast, a much longer average PL lifetime of ≈403 ns can be fitted by an bi-exponential decay curve (2.9 and 420 ns) for the $Cs_2AgIn_{0.9}Bi_{0.1}Cl_6$ NPLs (Figure 2E and Table S1, Supporting Information), in good accordance to the characteristic of STE emission due to its multi-step relaxation pathway as well as small wavefunction overlap between the excited and ground states.[29,42]

To further understand the optical behaviors of the $Cs_2AgIn_xBi_{1-x}Cl_6$ NPLs, we carried out the temperature-dependent steady-state and time-resolved PL measurements for the highly emissive $Cs_2AgIn_{0.9}Bi_{0.1}Cl_6$ double perovskite NPLs film (see the detail in the Supporting Information). As shown in **Figure 3**A, a pseudo-color contour map of the PL spectra showed a good preservation of the peak symmetricity at the temperature range of 10–330 K, excluding the possibility of exciton recombination through defect-related radiative pathways.[43] The integrated PL intensity showed a slight increase when increasing the temperature from 10 to ≈75K, which was attributed to the enhanced thermal-assisted charge carrier transfer from the conduction band minimum (CBM) to self-trapped states.[50] When further increasing the temperature, a continuous decrease of the PL intensity was observed which can be explained by the emergence of thermally activated non-radiative recombination processes (Figure 3B).[45] The PL peak position exhibited a monotonic blueshift upon increasing the temperature (Figure 3B), indicating that temperature-induced thermal expansion of the lattice rather than electron-phonon coupling was dominating the PL emission energy evolution of the $Cs_2AgIn_{0.9}Bi_{0.1}Cl_6$ double perovskite NPLs.[45–49]

It is known that exciton binding energy (E_b) plays an important role in the exciton dissociation and recombination processes. Therefore, we extracted the E_b value of the NPL sample based on the following equation:[19]

$$I(T) = \frac{I_0}{1 + A\exp\left(-\frac{E_b}{k_B T}\right)} \quad (1)$$

where I is the integrated intensity of each PL spectrum, T is the temperature, and k_B is the Boltzmann constant. An E_b value of 64.3 ± 6.8 meV was extracted by fitting the experimental result (Figure 3C), which was consistent with previous report,[50] and significantly smaller than the binding energies of LHP NPLs (i.e., 200–300 meV).[51] The low binding energy would facilitate exciton dissociation thus the carrier transfer to the self-trapped state for the subsequent STE emission process, well explaining the exhibited high PL QY (≈40%) of the sample. To understand further about the strength of electron-phonon interactions and radiative recombination process of the sample, we acquired the Huang–Rhys factor (S) and phonon energy ($\hbar\omega_{phonon}$) using the equation below:[44]

$$\mathrm{FWHM} = 2.36\sqrt{S}\hbar\omega_{phonon}\sqrt{\coth\frac{\hbar\omega_{phonon}}{2k_B T}} \quad (2)$$

where FWHM is full width at half maximum of the PL peak. By fitting the temperature dependent FWHM evolution (Figure 3D), the S and $\hbar\omega_{phonon}$ were determined to be 33.5 ± 0.2, and 36.0 ± 1.1 meV, respectively. The S value is larger than that of conventional semiconductors (e.g., 0.3 for ZnSe, 1 for CdSe, 3.2 for $CsPbBr_3$), [52,53] and smaller than the STEs perovskites (e.g., 79.5 for $Cs_3Bi_2I_9$, 50.4 for $Rb_3Sb_2I_9$).[44] Such moderate S factor can balance the electron-phonon coupling with excited-state energy dissipation through neighboring phonons, leading to the observed high PL QY.[19,44,54] Besides, we notice that the phonon energy ($\hbar\omega_{phonon}$) is close to the exciton binding energy (E_b), which may facilitate the process of phonon-mediated relaxation from CBM to self-trapped states and avoiding the radiative recombination of the band edge transition from CBM to valence band maximum (VBM).[55] Together, we believe that the low exciton binding energy along with the suitable S-factor and

 © 2023 Wiley-VCH GmbH

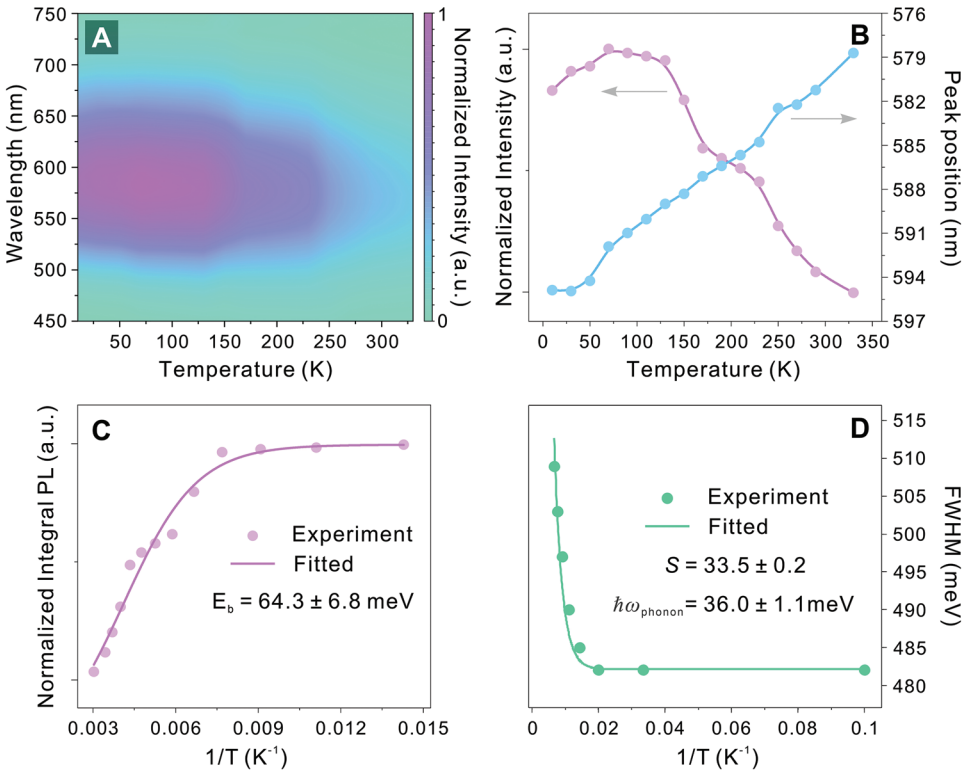

Figure 3. Temperature-dependent optical behaviors of the $Cs_2AgIn_{0.9}Bi_{0.1}Cl_6$ double perovskite NPLs. A) 2D pseudo-color contour map of normalized PL spectra as functions of temperature; B) integrated PL intensity and PL peak position as a function of temperature; C) temperature dependence of the integrated PL intensity with the corresponding Arrhenius fitting; D) temperature-dependence of the full width at half maximum (FWHM) of PL peak with the corresponding fitting result.

photon energy synergistically boost the STE emission thus PL QY of the 2D alloyed double perovskite NPLs.

Next, to unveil the morphological dimension reduction and In-Bi alloying effect on electronic structures of $Cs_2AgIn_xBi_{1-x}Cl_6$ ($0 \le x \le 1$) alloyed double perovskites, we then performed DFT calculations using general gradient approximation (GGA) with Perdew—Burke–Ernzerhof (PBE) as correlation functional (see calculation details in Supporting Information).[56] Three configurations of double perovskite atomic lattices, that is, 3D $Cs_2AgInCl_6$, 2D $Cs_2AgInCl_6$, and 2D $Cs_2AgIn_{0.75}Bi_{0.25}Cl_6$ were constructed for the calculation (Figure S13, Supporting Information). The calculated charge density difference showed that reducing the $Cs_2AgInCl_6$ double perovskite from 3D structure to 2D morphology did not cause a significant change for the charge transfer behavior (**Figure 4**A,B). In both cases, the charge mainly accumulated around the Cl atoms and in between the Cl and In atoms. When alloying Bi into the structure (i.e., $Cs_2AgIn_{0.75}Bi_{0.25}Cl_6$), a clear charge redistribution among the Bi–Cl–Ag can be visualized with increased charge accumulation between Cl and Ag atoms (Figure 4C).[57] Such charge redistributions can be quantitatively determined through the electron localization functional calculations (Figure 4D–F). The result showed that the morphological dimension reduction led to a 6.3% increase of the charge density between In and Cl (from 0.589 to 0.626, Figure S14, Supporting Information), indicating an enhanced covalent bonding character of the In—Cl bond. This charge density value was further increased to 0.639 when replacing 25% of In with Bi due to the enlarged charge accumulation on the In—Cl bond (Figure S14, Supporting Information). Such increased charge accumulation at the In—Cl bonds facilitated the overall charge carrier mobility and transfer dynamics of the system.[58]

The corresponding band structures and density of states of the three configurations were then calculated (Figure 4G–I and Figure S15, Supporting Information). Both VBM and CBM of the 3D $Cs_2AgInCl_6$ double perovskite located at the Γ symmetry point, resulting in a direct bandgap transition. However, the VBM, which is mainly contributed by Ag 4*d* orbitals, showed a flat band from Γ to *X* point.[59] The flat band structure resulted in a high effective mass of the holes (1.193 m_0, Table S2, Supporting Information), thus hindering the photogenerated carrier transfer and leading to the ease formation of deep intraband defect states.[29,60] Moreover, this low carrier mobility was consistent with the calculated squares of dipole transition matrix elements (Figure 4G), which showed a negligible value between VBM and CBM of the $Cs_2AgInCl_6$ double perovskite at Γ symmetry point (also because of the parity-forbidden transition).[28,41,59] The VBM flat band was changed to a clear peak feature when reducing the double perovskite dimension to a 2D configuration (Figure 4H). Accordingly, the hole effective mass was significantly decreased to 0.475 m_0 (Table S2, Supporting Information), facilitating the photocarrier interband transition. However, the dipole transition matrix calculation still showed a negligible value for the transition

© 2023 Wiley-VCH GmbH

15214095, 2023, 19, Downloaded from https://onlinelibrary.wiley.com/doi/10.1002/adma.202211235 by Brown University Library, Wiley Online Library on [12/05/2023]. See the Terms and Conditions (https://onlinelibrary.wiley.com/terms-and-conditions) on Wiley Online Library for rules of use; OA articles are governed by the applicable Creative Commons License

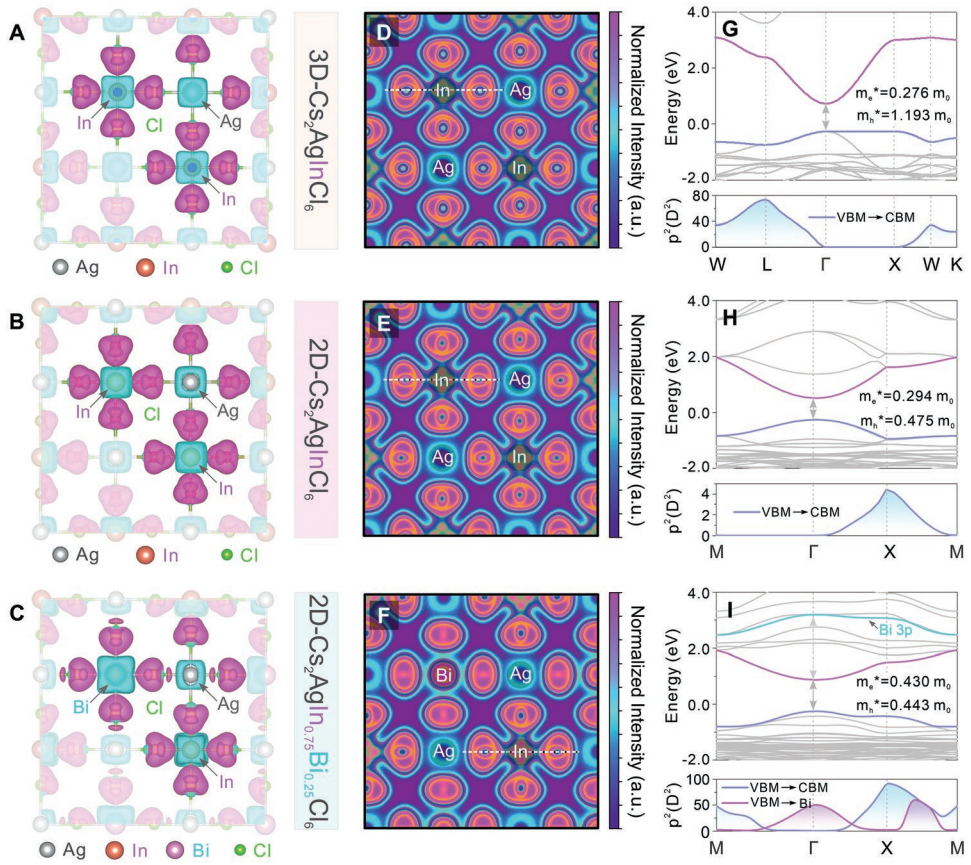

Figure 4. DFT calculation results of the 3D-$Cs_2AgInCl_6$, 2D-$Cs_2AgInCl_6$, and 2D- $Cs_2AgIn_{0.75}Bi_{0.25}Cl_6$ double perovskites. Charge density difference calculation of A) 3D-$Cs_2AgInCl_6$, B) 2D-$Cs_2AgInCl_6$, and C) 2D-$Cs_2AgIn_{0.75}Bi_{0.25}Cl_6$, the purple and cyan surfaces represent for the charge gain and the equivalent charge loss, respectively; Electron localization functional analysis of D) 3D-$Cs_2AgInCl_6$, E) 2D-$Cs_2AgInCl_6$, and F) 2D-$Cs_2AgIn_{0.75}Bi_{0.25}Cl_6$; calculated band structures (top panel) and the corresponding squares of dipole transition matrix elements (bottom panel) of G) 3D-$Cs_2AgInCl_6$, H) 2D-$Cs_2AgInCl_6$, and I) 2D-$Cs_2AgIn_{0.75}Bi_{0.25}Cl_6$ double perovskites.

probability at Γ point (Figure 4H), largely due to the preservation of the symmetry-induced parity-forbidden transition of the $Cs_2AgInCl_6$ double perovskite. These results are in good agreement with the observed weak band-edge absorption and weak emission with a direct bandgap transition nature of the pure $Cs_2AgInCl_6$ NPLs (Figure 2A). Upon alloying 25% of Bi to the double perovskite configuration (i.e., $Cs_2AgIn_{0.75}Bi_{0.25}Cl_6$), the hole effective mass further decreased to 0.443 m_0 (Figure 4I and Table S2, Supporting Information). Both the reduced hole effective mass and the loss of inversion center (thus relaxing the parity selection rule) due to In−Bi alloying concurrently led to a drastically increased electron transition probability to the Bi sites in conduction band based on the squares of dipole transition matrix elements calculation (Figure 4I). In this case, the excited electrons can relax to the STE state through CBM of the $Cs_2AgIn_{0.75}Bi_{0.25}Cl_6$ double perovskite for subsequent radiative recombination with holes. Together, all the calculation results revealed that both the morphological dimension reduction (from 3D particles to 2D platelets) and alloying a small amount of Bi into the $Cs_2AgInCl_6$ double perovskite lattice co-played the role of facilitating photocarrier transfer dynamics of the alloyed double perovskite NPLs, well explaining the experimentally observed high PL QY of the $Cs_2AgIn_{0.9}Bi_{0.1}Cl_6$ NPLs.

Stability of any optoelectronic materials is crucially important for practical applications. To evaluate the stability of the double perovskite NPLs synthesized here, we monitored the optical and structural properties of the $Cs_2AgIn_{0.9}Bi_{0.1}Cl_6$ NPLs in toluene solution as well as $Cs_2AgIn_{0.9}Bi_{0.1}Cl_6$ NPLs-based solid thin films. For the toluene solution storage, the sample showed no obvious changes in both optical properties and crystal structure after storage over a month (Figure S16, Supporting Information). For the thin-film sample, upon storage under ambient conditions for at least 25 days, the NPLs exhibited minimal variations in their PL profiles, and 15–20% increase in the PL QY after storing for 15 days (**Figure 5**A,B). This PL QY increase can be ascribed to the effective surface passivation induced by the formation of surface perovskite hydrate through absorbing moisture in air, in line with previous findings for other lead-free perovskite NCs.[61,62] In addition, no measurable change in the crystal structure was observed (Figure 5C), further demonstrating the superior ambient stability of the sample. Next, we tested the stability of the NPL thin film by immersing the film in different polar solvents. After immersing for about one minute, 23% increase, and 9%, and 11% decreases in the PL QY were observed for the samples immersed in water, acetone, and ethanol,

© 2023 Wiley-VCH GmbH

15214095, 2023, 19, Downloaded from https://onlinelibrary.wiley.com/doi/10.1002/adma.202211235 by Brown University Library, Wiley Online Library on [12/05/2023]. See the Terms and Conditions (https://onlinelibrary.wiley.com/terms-and-conditions) on Wiley Online Library for rules of use; OA articles are governed by the applicable Creative Commons License

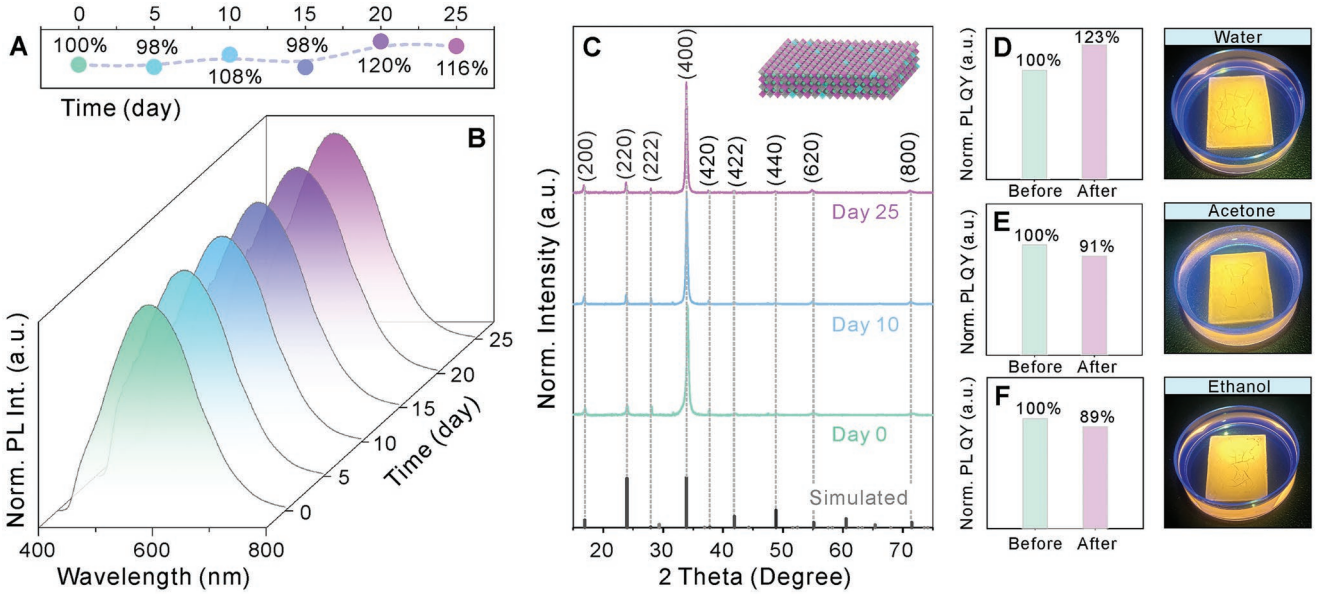

Figure 5. Stability tests of the $Cs_2AgIn_{0.9}Bi_{0.1}Cl_6$ double perovskite NPL film. A) PL intensity variation of the $Cs_2AgIn_{0.9}Bi_{0.1}Cl_6$ NPL film under ambient conditions for 25 days (normalized to the initial PL intensity of the sample); B) the corresponding normalized (Norm.) PL spectra of the NPL film at different storage time; C) XRD patterns of the alloyed double perovskite NPL film at 0, 10, 25 days; D–F) normalized PL QYs of the $Cs_2AgIn_{0.9}Bi_{0.1}Cl_6$ NPL films before and after immersing in D) water, E) acetone, and F) ethanol, right panels are photographs of the NPL film immersed in different polar solvents under 365 nm light excitation.

respectively (Figure 5D–F), exhibiting robustness of the NPLs against common polar solvents. Together, the results unequivocally demonstrated an excellent stability of the $Cs_2AgIn_xBi_{1-x}Cl_6$ alloyed double perovskite NPLs, rendering them highly adaptable especially for device integrations through all solution-processing techniques.

At last, to demonstrate the device application potential of the $Cs_2AgIn_xBi_{1-x}Cl_6$ alloyed double perovskite NPLs, we solution-processed an NPL-based LED (NPL-LED) device using $Cs_2AgIn_{0.9}Bi_{0.1}Cl_6$ NPLs with the device structure of ITO/PEDOT:PSS/TFB/PVK:NPLs/ZnO/Al (**Figure 6**A,B and Figures S17, S18, Supporting Information). The positions of

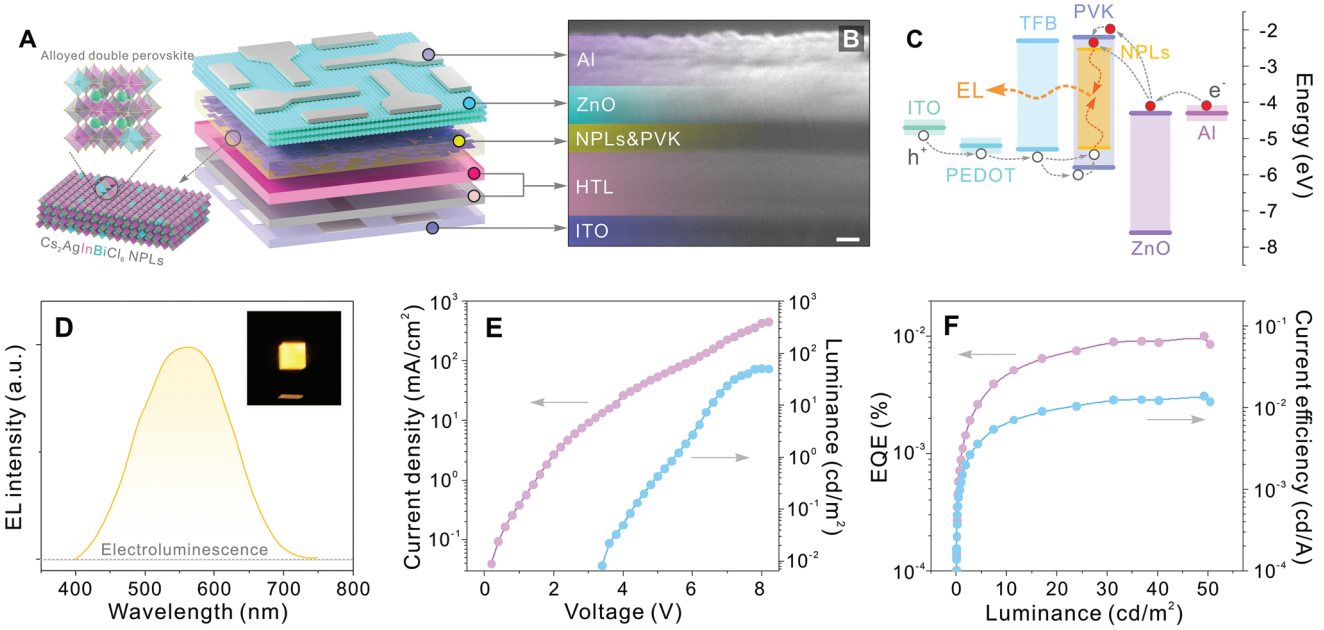

Figure 6. Performance characterizations of all solution-processed $Cs_2AgIn_{0.9}Bi_{0.1}Cl_6$ NPL-based LED. A) The device structure schematic of the NPL-LED; B) a cross section SEM image of the NPL-LED device; C) band alignments and proposed charge carrier transfer processes of the NPL-LED; D) Electroluminescence (EL) spectrum of the LED; E) the corresponding current density-voltage-luminance curves, and F) external quantum efficiency (EQE) and current efficiency as a function of luminance of the NPL-LED.

© 2023 Wiley-VCH GmbH

15214095, 2023, 19, Downloaded from https://onlinelibrary.wiley.com/doi/10.1002/adma.202211235 by Brown University Library, Wiley Online Library on [12/05/2023]. See the Terms and Conditions (https://onlinelibrary.wiley.com/terms-and-conditions) on Wiley Online Library for rules of use; OA articles are governed by the applicable Creative Commons License

VBM and CBM were determined to be 5.61 and 2.53 eV based on ultraviolet photoelectron spectroscopy analyses (Figure 6C, see the details in Figure S19, Supporting Information). It is noted that 25 wt% of PVK was applied in the emissive layer to promote the NPL dispersity while acting as a buffer component to prevent electron leakage into the TFB layer (Figures S20 and S21, Supporting Information). The final NPL-LED device exhibited a uniform working area (Figure 6D inset), and the electroluminescence (EL) spectrum showed a broad peak maximized at 557 nm, consistent with the PL peak profile of the $Cs_2AgIn_{0.9}Bi_{0.1}Cl_6$ NPLs in solution (Figure 6D and Figure 2A). This result indicated that the STE emission rather than impurity/surface states of the NPLs or other functional layers served as the sole EL origin. In addition, the turn-on voltage of 5.5 V (1 cd m^{-2}) was much lower than that reported in previous works (i.e., ≈10 V),[19,29] and the luminance maximum (58 cd m^{-2}) of the NPL-LED device was comparable to that of the LED devices fabricated through the state-of-the-art thermal evaporation technique using similar materials.[19] The external quantum efficiency (EQE, ≈0.01%) and current efficiency (≈0.013 cd A^{-1}) showed a plateau performance across a wide range of luminance (Figure 6E), demonstrating its high resistance to the roll-off effect for the fabricated NPL-LED device.

In summary, we demonstrate a controlled synthesis of lead-free $Cs_2AgIn_xBi_{1-x}Cl_6$ ($0 \le x \le 1$) alloyed double perovskite NPLs with PL QYs reaching as high as 40.1%. Experimental results and theoretical calculations prove that both the morphological dimension reduction and In−Bi alloying effect are responsible for the superior optical performances of the NPLs. Moreover, these NPLs show high stability against moisture and polar solvents, which allows for the ease fabrication of optoelectronic devices through facile and cost-effective solution-processing techniques. For the first time, we fabricated an all-solution-processed LED device using $Cs_2AgIn_{0.9}Bi_{0.1}Cl_6$ NPLs, which shows a pure EL solely from the STE state of the applied alloyed NPLs. The produced device exhibits a comparable performance to the state-of-the-art LED devices fabricated through thermal evaporation process using lead-free double perovskite as emitter. Our study not only demonstrates the synthesis and application potentials of 2D alloyed double perovskite NPLs, but also sheds important lights on future developments and implementations of lead-free perovskite materials in cost-efficient and low-toxic optoelectronic devices.

Supporting Information

Supporting Information is available from the Wiley Online Library or from the author.

Acknowledgements

Z.L., A.T., and L.G. acknowledge the support from National Natural Science Foundation of China (Nos. 62205098, 61974009, and 62075055). O.C. acknowledges the support from the Brown University startup fund and 3M Foundation through the Non-Tenured Faculty Award program.

Note: Marking to indicate Aiwei Tang as a second corresponding author was added on May 11, 2023, after initial publication online.

Conflict of Interest

The authors declare no conflict of interest.

Author Contributions

Z.L. and O.C. conceived the idea. Z.L., Y.S., and T.C. carried out the synthesis of the NPLs and most of characterizations. Y.S. conducted the stability experiment. J.Z. X.L., and A.T. constructed and characterized the LEDs. T.Y., X.L., L.G., W.S., and X.Z. contributed to the computation part. M.C. conducted the TEM-related measurements. H.Y. analyzed the temperature dependent PL spectra. X.L. conducted the XRD measurement. Z.L. and O.C. wrote the manuscript and all authors commented on the manuscript. O.C. supervised the entire project.

Data Availability Statement

The data that support the findings of this study are available from the corresponding author upon reasonable request.

Keywords

2D materials, alloyed double perovskites, lead-free perovskites, light-emitting diodes, solution-processing

Received: December 1, 2022
Revised: February 21, 2023
Published online: March 27, 2023

[1] A. Kojima, K. Teshima, Y. Shirai, T. Miyasaka, *J. Am. Chem. Soc.* **2009**, *131*, 6050.
[2] J. Burschka, N. Pellet, S. J. Moon, R. Humphry-Baker, P. Gao, M. K. Nazeeruddin, M. Gratzel, *Nature* **2013**, *499*, 316.
[3] H. Min, D. Y. Lee, J. Kim, G. Kim, K. S. Lee, J. Kim, M. J. Paik, Y. K. Kim, K. S. Kim, M. G. Kim, T. J. Shin, S. Il Seok, *Nature* **2021**, *598*, 444.
[4] Y. Dong, Y. K. Wang, F. Yuan, A. Johnston, Y. Liu, D. Ma, M. J. Choi, B. Chen, M. Chekini, S. W. Baek, L. K. Sagar, J. Fan, Y. Hou, M. Wu, S. Lee, B. Sun, S. Hoogland, R. Quintero-Bermudez, H. Ebe, P. Todorovic, F. Dinic, P. Li, H. T. Kung, M. I. Saidaminov, E. Kumacheva, E. Spiecker, L. S. Liao, O. Voznyy, Z. H. Lu, E. H. Sargent, *Nat. Nanotechnol.* **2020**, *15*, 668.
[5] X. K. Liu, W. Xu, S. Bai, Y. Jin, J. Wang, R. H. Friend, F. Gao, *Nat. Mater.* **2021**, *20*, 10.
[6] S. Cong, G. Zou, Y. Lou, H. Yang, Y. Su, J. Zhao, C. Zhang, P. Ma, Z. Lu, H. Fan, Z. Huang, *Nano Lett.* **2019**, *19*, 3676.
[7] L. Protesescu, S. Yakunin, M. I. Bodnarchuk, F. Krieg, R. Caputo, C. H. Hendon, R. X. Yang, A. Walsh, M. V. Kovalenko, *Nano Lett* **2015**, *15*, 3692.
[8] Q. Zhou, Z. Bai, W. G. Lu, Y. Wang, B. Zou, H. Zhong, *Adv. Mater.* **2016**, *28*, 9163.
[9] K. Zheng, Q. Zhu, M. Abdellah, M. E. Messing, W. Zhang, A. Generalov, Y. Niu, L. Ribaud, S. E. Canton, T. Pullerits, *J. Phys. Chem. Lett.* **2015**, *6*, 2969.
[10] Z. G. Xiao, R. A. Kerner, L. F. Zhao, N. L. Tran, K. M. Lee, T. W. Koh, G. D. Scholes, B. P. Rand, *Nat. Photonics* **2017**, *11*, 108.
[11] Z. Chu, Y. Zhao, F. Ma, C. X. Zhang, H. Deng, F. Gao, Q. Ye, J. Meng, Z. Yin, X. Zhang, J. You, *Nat. Commun.* **2020**, *11*, 4165.
[12] A. Babayigit, A. Ethirajan, M. Muller, B. Conings, *Nat. Mater.* **2016**, *15*, 247.
[13] P. Docampo, T. Bein, *Acc. Chem. Res.* **2016**, *49*, 339.
[14] H. Yang, Y. Zhang, K. Hills-Kimball, Y. Zhou, O. Chen, *Sustainable Energy Fuels* **2018**, *2*, 2381.
[15] Y. Liu, A. Nag, L. Manna, Z. Xia, *Angew Chem. Int. Ed. Engl.* **2021**, *60*, 11592.

© 2023 Wiley-VCH GmbH

15214095, 2023, 19, Downloaded from https://onlinelibrary.wiley.com/doi/10.1002/adma.202211235 by Brown University Library, Wiley Online Library on [12/05/2023]. See the Terms and Conditions (https://onlinelibrary.wiley.com/terms-and-conditions) on Wiley Online Library for rules of use; OA articles are governed by the applicable Creative Commons License

[16] C. N. Savory, A. Walsh, D. O. Scanlon, *ACS Energy Lett.* **2016**, *1*, 949.
[17] A. H. Slavney, T. Hu, A. M. Lindenberg, H. I. Karunadasa, *J. Am. Chem. Soc.* **2016**, *138*, 2138.
[18] Y. Bekenstein, J. C. Dahl, J. Huang, W. T. Osowiecki, J. K. Swabeck, E. M. Chan, P. Yang, A. P. Alivisatos, *Nano Lett.* **2018**, *18*, 3502.
[19] J. Luo, X. Wang, S. Li, J. Liu, Y. Guo, G. Niu, L. Yao, Y. Fu, L. Gao, Q. Dong, C. Zhao, M. Leng, F. Ma, W. Liang, L. Wang, S. Jin, J. Han, L. Zhang, J. Etheridge, J. Wang, Y. Yan, E. H. Sargent, J. Tang, *Nature* **2018**, *563*, 541.
[20] T. Cai, W. Shi, S. Hwang, K. Kobbekaduwa, Y. Nagaoka, H. Yang, K. Hills-Kimball, H. Zhu, J. Wang, Z. Wang, Y. Liu, D. Su, J. Gao, O. Chen, *J. Am. Chem. Soc.* **2020**, *142*, 11927.
[21] F. Locardi, M. Cirignano, D. Baranov, Z. Dang, M. Prato, F. Drago, M. Ferretti, V. Pinchetti, M. Fanciulli, S. Brovelli, L. De Trizio, L. Manna, *J. Am. Chem. Soc.* **2018**, *140*, 12989.
[22] H. Yang, T. Cai, L. Dube, O. Chen, *Chem. Sci.* **2022**, *13*, 4874.
[23] T. Cai, W. Shi, D. J. Gosztola, K. Kobbekaduwa, H. Yang, N. Jin, Y. Nagaoka, L. Dube, J. Schneider, S. Hwang, J. Gao, X. Ma, O. Chen, *Matter* **2021**, *4*, 2936.
[24] N. Chen, T. Cai, W. Li, K. Hills-Kimball, H. Yang, M. Que, Y. Nagaoka, Z. Liu, D. Yang, A. Dong, C. Y. Xu, R. Zia, O. Chen, *ACS Appl. Mater. Interfaces* **2019**, *11*, 16855.
[25] A. Karmakar, M. S. Dodd, S. Agnihotri, E. Ravera, V. K. Michaelis, *Chem. Mater.* **2018**, *30*, 8280.
[26] B. Yang, X. Mao, F. Hong, W. Meng, Y. Tang, X. Xia, S. Yang, W. Deng, K. Han, *J. Am. Chem. Soc.* **2018**, *140*, 17001.
[27] Y. Liu, Y. Jing, J. Zhao, Q. Liu, Z. Xia, *Chem. Mater.* **2019**, *31*, 3333.
[28] A. Karmakar, G. M. Bernard, A. Meldrum, A. O. Oliynyk, V. K. Michaelis, *J. Am. Chem. Soc.* **2020**, *142*, 10780.
[29] Y. Zhang, Z. Zhang, W. Yu, Y. He, Z. Chen, L. Xiao, J. J. Shi, X. Guo, S. Wang, B. Qu, *Adv. Sci.* **2022**, *9*, 2102895.
[30] Z. Liu, J. Zito, M. Ghini, L. Goldoni, M. Prato, H. Bahmani Jalali, I. Infante, L. De Trizio, L. Manna, *Nano Lett.* **2022**, *22*, 8567.
[31] H. T. Chen, H. Y. Xiang, Y. T. Zou, S. Zhang, B. Cai, J. B. Zhang, L. T. Hou, H. B. Zeng, *Adv. Opt. Mater.* **2022**, *10*, 2200510.
[32] J. Song, L. Xu, J. Li, J. Xue, Y. Dong, X. Li, H. Zeng, *Adv. Mater.* **2016**, *28*, 4861.
[33] Z.-J. Li, E. Hofman, A. H. Davis, M. M. Maye, W. Zheng, *Chem. Mater.* **2018**, *30*, 3854.
[34] Z. Liu, H. Yang, J. Wang, Y. Yuan, K. Hills-Kimball, T. Cai, P. Wang, A. Tang, O. Chen, *Nano Lett.* **2021**, *21*, 1620.
[35] C. F. Holder, R. E. Schaak, *ACS Nano* **2019**, *13*, 7359.
[36] J. Zhou, Z. G. Xia, M. S. Molokeev, X. W. Zhang, D. S. Peng, Q. L. Liu, *J. Mater. Chem.* **2017**, *5*, 15031.
[37] P. G. Han, X. Zhang, X. Mao, B. Yang, S. Q. Yang, Z. C. Feng, D. H. Wei, W. Q. Deng, T. Pullerits, K. L. Han, *Sci. China Chem.* **2019**, *62*, 1405.
[38] M. Zhang, L. Zhao, J. Xie, Q. Zhang, X. Wang, N. Yaqoob, Z. Yin, P. Kaghazchi, S. Zhang, H. Li, C. Zhang, L. Wang, L. Zhang, W. Xu, J. Xing, *Nat. Commun.* **2021**, *12*, 4890.
[39] F. Locardi, E. Sartori, J. Buha, J. Zito, M. Prato, V. Pinchetti, M. L. Zaffalon, M. Ferretti, S. Brovelli, I. Infante, L. De Trizio, L. Manna, *ACS Energy Lett.* **2019**, *4*, 1976.
[40] Z. Yuan, C. Zhou, Y. Tian, Y. Shu, J. Messier, J. C. Wang, L. J. Van De Burgt, K. Kountouriotis, Y. Xin, E. Holt, K. Schanze, R. Clark, T. Siegrist, B. Ma, *Nat. Commun.* **2017**, *8*, 14051.
[41] J. Luo, S. Li, H. Wu, Y. Zhou, Y. Li, J. Liu, J. Li, K. Li, F. Yi, G. Niu, J. Tang, *ACS Photonics* **2017**, *5*, 398.
[42] B. Yang, L. Yin, G. Niu, J. H. Yuan, K. H. Xue, Z. Tan, X. S. Miao, M. Niu, X. Du, H. Song, E. Lifshitz, J. Tang, *Adv. Mater.* **2019**, *31*, 1904711.
[43] F. Zhang, H. Zhong, C. Chen, X. G. Wu, X. Hu, H. Huang, J. Han, B. Zou, Y. Dong, *ACS Nano* **2015**, *9*, 4533.
[44] K. M. Mccall, C. C. Stoumpos, S. S. Kostina, M. G. Kanatzidis, B. W. Wessels, *Chem. Mater.* **2017**, *29*, 4129.
[45] Z. Ma, Z. Shi, C. Qin, M. Cui, D. Yang, X. Wang, L. Wang, X. Ji, X. Chen, J. Sun, D. Wu, Y. Zhang, X. J. Li, L. Zhang, C. Shan, *ACS Nano* **2020**, *14*, 4475.
[46] C. L. Yu, Z. Chen, J. J. Wang, W. Pfenninger, N. Vockic, J. T. Kenney, K. Shum, *J. Appl. Phys.* **2011**, *110*, 063526.
[47] H. J. Lian, A. Yang, M. L. W. Thewalt, R. Lauck, M. Cardona, *Phys. Rev. B* **2006**, *73*, 233202.
[48] D. Zhang, S. W. Eaton, Y. Yu, L. Dou, P. Yang, *J. Am. Chem. Soc.* **2015**, *137*, 9230.
[49] J. Zhang, Y. Yang, H. Deng, U. Farooq, X. Yang, J. Khan, J. Tang, H. Song, *ACS Nano* **2017**, *11*, 9294.
[50] A. Yangui, D. Garrot, J. S. Lauret, A. Lusson, G. Bouchez, E. Deleporte, S. Pillet, E. E. Bendeif, M. Castro, S. Triki, Y. Abid, K. Boukheddaden, *J. Phys. Chem. C* **2015**, *119*, 23638.
[51] S. Wang, J. Qi, S. V. Kershaw, A. L. Rogach, *ACS Nanosci. Au* **2021**, *2*, 93.
[52] H. Zhao, H. Kalt, *Phys. Rev. B* **2003**, *68*, 125309.
[53] X. Lao, Z. Yang, Z. Su, Z. Wang, H. Ye, M. Wang, X. Yao, S. Xu, *Nanoscale* **2018**, *10*, 9949.
[54] X. Zhao, G. Niu, J. Zhu, B. Yang, J. H. Yuan, S. Li, W. Gao, Q. Hu, L. Yin, K. H. Xue, E. Lifshitz, X. Miao, J. Tang, *J. Phys. Chem. Lett.* **2020**, *11*, 1873.
[55] J. Pal, A. Bhunia, S. Chakraborty, S. Manna, S. Das, A. Dewan, S. Datta, A. Nag, *J. Phys. Chem.* **2018**, *122*, 10643.
[56] J. P. Perdew, K. Burke, M. Ernzerhof, *Phys. Rev. Lett.* **1996**, *77*, 3865.
[57] Y.-K. Jung, K. T. Butler, A. Walsh, *J. Phys. Chem.* **2017**, *121*, 27351.
[58] W. Shi, T. Cai, Z. Wang, O. Chen, *J. Chem. Phys.* **2020**, *153*, 141101.
[59] W. Meng, X. Wang, Z. Xiao, J. Wang, D. B. Mitzi, Y. Yan, *J. Phys. Chem. Lett.* **2017**, *8*, 2999.
[60] G. Volonakis, A. A. Haghighirad, R. L. Milot, W. H. Sio, M. R. Filip, B. Wenger, M. B. Johnston, L. M. Herz, H. J. Snaith, F. Giustino, *J. Phys. Chem. Lett.* **2017**, *8*, 772.
[61] B. Yang, J. Chen, F. Hong, X. Mao, K. Zheng, S. Yang, Y. Li, T. Pullerits, W. Deng, K. Han, *Angew Chem. Int. Ed. Engl.* **2017**, *56*, 12471.
[62] Z. Z. Ma, Z. F. Shi, L. T. Wang, F. Zhang, D. Wu, D. W. Yang, X. Chen, Y. Zhang, C. X. Shan, X. J. Li, *Nanoscale* **2020**, *12*, 3637.

© 2023 Wiley-VCH GmbH

15214095, 2023, 19, Downloaded from https://onlinelibrary.wiley.com/doi/10.1002/adma.202211235 by Brown University Library, Wiley Online Library on [12/05/2023]. See the Terms and Conditions (https://onlinelibrary.wiley.com/terms-and-conditions) on Wiley Online Library for rules of use; OA articles are governed by the applicable Creative Commons License